A Channel Propagation Model for the 700 MHz Band

Camillo Gentile & Nada Golmie
Advanced Network Technologies Division
NIST
Gaithersburg, Maryland

Kate A. Remley & Chris L. Holloway
Electromagnetics Division
NIST
Boulder, Colorado

William F. Young
Wireless & Event Sensing Applications
Sandia National Laboratories
Albuquerque, New Mexico

***Abstract*— Conversion from analog television in the United States combined with the appeal for broadband public safety communications is generating a lot of interest in the so-called 700 MHz band between 698-806 MHz. To our knowledge, no channel propagation model for this band exists to date. In this work, we derive such a model reduced from a measurement campaign realized through a stepped-frequency system. The campaign includes 89 transmitter-receiver configurations in seven different environments relevant to residential, commercial and public safety communications, ranging from subterranean mine tunnels to an oil refinery, from mid-size to high-rise buildings. The stochastic impulse response model is complete with 17 parameters which enables reconstruction for use in simulation engines, amongst others.**

***Index Terms*— Public safety bands; LTE**

I. Introduction

The conversion from analog television in the United States combined with the appeal for broadband pubic safety communications, is generating a lot of interest in the 700 MHz band. Thus, the 764-776 MHz and 794-806 MHz blocks have been dedicated to public safety while the others have been auctioned off to vendors for commercial services, and some blocks for joint use between the two [1]. This so-called 700 MHz band offers excellent penetration through buildings, which is particularly useful for emergency responders and Enhanced 911 services. For commercial vendors, the investment is motivated by the favorable propagation characteristics which extend coverage significantly for the same transmission power, translating into less infrastructure: while it requires nine cells at 2400 MHz and four cells at 1900 MHz to span 100 m^2, it is projected to require only one cell at 700 MHz [2].

However before any network technology can be developed and deployed in this band, there is a need to characterize and understand the propogation environment in which it must operate.

To our knowledge, no channel propagation model for the 700 MHz band exists in the open literature to date. In this work, we derive such a model, reduced from a measurement campaign conducted in seven different environments relevant to most usage scenarios, ranging from subterranean mine tunnels to an oil refinery, from mid-size to high-rise buildings.

The paper reads as follows: Section II describes the stepped-frequency technique used to measure the propagation channel between a transmitter and receiver. The subsequent section explains our measurement system realized through a vector network analyzer, and outlines the campaign. Section IV features the proposed stochastic model characterizing the channel impulse response with parameters reported individually for each environment. The last section summarizes our results.

[0]This work was funded by the Public Safety Communications Research Lab through NIST's Office of Law Enforcement Standards.

[0]Members of the NIST RF Fields Group technical staff conducted the measurement campaigns described here.

II. The Channel Impulse Response

The impulse response $h(t)$ characterizes the static propagation channel, appropriate for use in public-safety applications where responders move slowly and in stages through a structure. It is composed from an infinite number of multipath arrivals indexed through k

$$h(t) := \sum_{k=1}^{\infty} a_k e^{j\varphi_k} \delta(t - \tau_k), \tag{1}$$

where τ_k denotes the delay of the arrival in propagation between the transmitter and receiver and the complex-amplitude $a_k e^{j\varphi_k}$ accounts for attenuation and phase change due to reflection, diffraction, and other specular effects introduced by walls (and other objects) on its path.

The impulse response has a frequency response

$$H(f) = \sum_{k=1}^{\infty} a_k e^{j\varphi_k} e^{-j2\pi f \tau_k}, \tag{2}$$

suggesting that the channel can be characterized through the stepped-frequency technique. We sample $H(f) = \frac{Y(f)}{X(f)}$ at rate Δf by transmitting tones $X(f)$ across the channel and then measuring $Y(f)$ at the receiver. Characterizing the channel in the frequency domain offers an advantage over transmitting a UWB pulse and recording the impulse response directly: a subband with bandwidth B and center frequency f_c can be selected a posteriori in reconstructing the channel. The discrete frequency spectrum $X(f)$ transforms to a signal with period $\frac{1}{\Delta f}$ in the time domain [3], and so choosing

Presented at the IEEE International Conference on Communications 2010

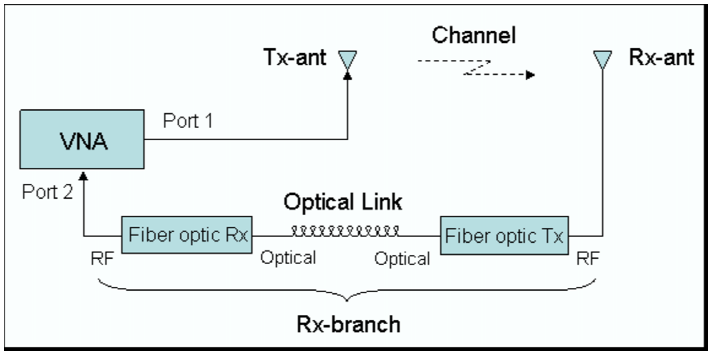

(a) Block diagram

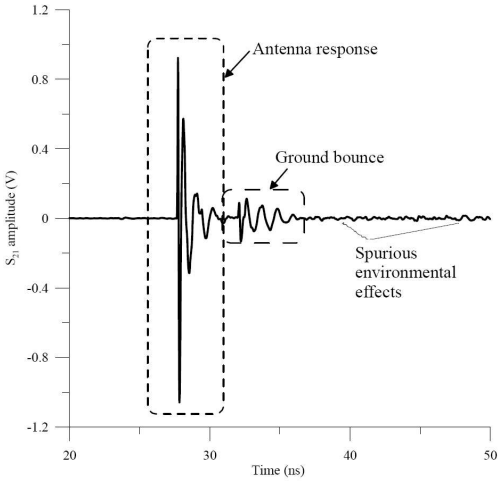

(b) Time-gating in the calibration step

Fig. 1. The stepped-frequency measurement technique using a vector network analyzer.

Δf = 0.375 MHz allows for a maximum multipath spread of 2667 ns which proves sufficient throughout all seven environments for the arrivals to subside within one period and avoid time aliasing.

The impulse response $h(t)$ can then be recovered through the Inverse Discrete Fourier Transform (IDFT) of the frequency response by synthesizing all the frequencies in the subband as

$$h(t) = \frac{1}{\frac{B}{\Delta f}} \sum_{l=1}^{\frac{B}{\Delta f}} H(f) e^{j2\pi f t}, \tag{3}$$

where $f = f_c - \frac{B}{2} + l \cdot \Delta f$.

III. The Measurement System and Campaign

A. The measurement system

Fig. 1(a) displays the block diagram of our measurement system. As explained in the previous section, the vector network analyzer (VNA) emits a series of tones with frequency f at Port 1 and measures the relative complex amplitude $S^{21}(f)$ at Port 2 with respect to Port 1, providing automatic synchronization between the two. The 200 m optical link enables measurement of the one-way propagation channel for variable placement of the transmitter and receiver antennas from each other throughout the test area. The optical fiber itself combines ultra-low loss and dispersion up to 100 GHz frequencies with immunity to electrical interference, preventing cross-talk between cables and pickup of environmental noise. The identical discone transmit and receive antennas were mounted on tripods with height fixed of 1.5 m and the output power at Port 1 was set to -13 dBm. After radiating from the transmitter, the signal propagates across the channel. Once detected by the receiver, it passes through the optical link before being fed back to Port 2.

The $S^{21}(f)$-parameter of the network in Fig. 1(a) can be expressed as a product of the Tx-antenna, the propagation channel H, the Rx-antenna, and the Rx-branch:

$$S^{21}(f) = H_{Tx}^{ant}(f) \cdot H(f) \cdot H_{Rx}^{ant}(f) \cdot H_{Rx}^{bra}(f) \tag{4}$$

The reponse H_{Rx}^{bra}, including the non-ideal VNA electronics, connectors, cables, amplifiers, and optical fiber link, is calibrated out using a standard VNA calibration technique where known impedance standards are connected sequentially at both ports. The response of the antennas and their connecting cables, H_{Tx}^{ant} and H_{Rx}^{ant}, are calibrated out in a subsequent step by separating the antennas by 3 m[1] and recording the free-space parameter S_{Fs}^{21} for which $H = H_{Fs}$, the response of the 3 m free-space channel. S_{Fs}^{21} is subsequently time-gated to remove both the ground bounce between the antennas and the spurious environmental effects as shown in Fig. 1(b). Finally the sought measured response H between any transmitter-receiver configuration can be extracted from the measured parameter S^{21} by dividing it by the free-space parameter such that $H = \frac{S^{21} \cdot H_{Fs}}{S_{Fs}^{21}}$, which also accounts for H_{Fs} given through the Friis transmission equation [4]. Complete details of the measurement system are available in [5].

B. The measurement campaign

The measurement campaign was conducted in several different environments in Colorado and California [5], [6], as summarized in Table I. A total of 89 experiments were recorded mostly in non-line-of-sight conditions, except for a few in the mine tunnels. As the environments are representative of public safety scenarios, the majority

[1]This ensures operation within the far-field of the antennas while minimizing environmental reflections.

was taken by placing the transmitter outside, typically at a command post, and the receiver inside, simulating an emergency responder. The ground-truth distance d between the transmitter and receiver was recorded for each experiment.

TABLE I
EXPERIMENTS CONDUCTED IN THE MEASUREMENT CAMPAIGN

environment	location	range (m)	Tx-Rx config.
Oil Refinery	Commerce City CO	33.8-135.4	outside–outside[2]
Greathouse Mine Tunnel	Antioch, CA	4.7-101.4	inside–inside
Hazel-Atlas Mine Tunnel	Antioch, CA	4.3-114.2	outside–inside
Horizon West Apartments	Boulder, CO	59.1-107.7	outside–inside
NIST Lab	Boulder, CO	54.2-137.6	outside–inside
Convention Center	Denver, CO	13.4-189.6	outside–inside
Republic Plaza[3]	Denver, CO	12.7-52.0	outside–inside

IV. THE PROPOSED CHANNEL PROPAGATION MODEL

This section describes the proposed channel propagation model. It is divided into two components: 1) the *reference impulse response* characterizes the shape of the multipath profile $h(t)$ while 2) the *pathgain* scales its amplitude according to the distance between the transmitter and receiver. The two corresponding subsections explain the extraction and modeling of the parameters of each component, following by a subsection that outlines in pseudocode how to employ the parameters to generate a stochastic impulse response in each of the environments.

A. The pathgain model

The *excess* pathgain[4] is defined as

$$PG(d) := \frac{1}{\frac{B}{\Delta f}} \sum_{l=1}^{\frac{B}{\Delta f}} |H(f)|^2, \tag{5}$$

where $f = f_c - \frac{B}{2} + l \cdot \Delta f$. Each data point is computed from the measured frequency response for f = 698–806 MHz from an experiment with distance d. In order to generate a model for the pathgain, consider decomposing the arrival amplitude in (2)

$$a_k = \tilde{a}_k \left(\frac{d}{d_0} \right)^{-\frac{n}{2}} \tag{6}$$

as a product of the *reference amplitude* $\tilde{a}_k$ valid at reference point d_0 and the *pathgain factor* representing the distance dependence of the amplitude. By substituting (2) into (5) and expanding, the pathgain model can be written as

$$\begin{aligned} (a) \quad PG(d) &= PG(d_0) \left(\frac{d}{d_0} \right)^{-n} \quad ; \\ (b)\ PG(d_0) &= \sum_{k=1}^{\infty} \tilde{a}_k^2. \end{aligned} \tag{7}$$

The *reference pathgain* $PG(d_0)$ for d_0 = 1 m and the attenuation coefficient n were extracted by robust fitting[5] of the model above to the data points from (5). We actually found the breakpoint model [8]

$$PG(d) = \begin{cases} PG(d_0) \left(\frac{d}{d_0} \right)^{-n_0} \cdot 10^{\frac{s_d}{10}} \ , \ d \le d_1 \\ \\ PG(d_1) \left(\frac{d}{d_1} \right)^{-n_1} \cdot 10^{\frac{s_d}{10}} \ , \ d > d_1 \end{cases} \tag{8}$$

to represent the data more accurately in some environments. For example, in the mine tunnel environments, the first segment for $d \le d_1$ were in line-of-sight conditions while in the second segment the receiver was positioned around a corner passage and so in non-line-of-sight conditions. As well, in *Oil Refinery*, the first segment was also in line-of-sight conditions however in the second a train of large metal columns obstructed the receiver.

The pathgain in (8) is augmented by the well-established parameter $s_d \sim \mathcal{N}(s_d; 0, \sigma_d)$, normally distributed, which quantifies the variation between our model and the data points and in that capacity represents the stochastic nature of the pathgain. This is of particular use when simulating time diversity systems [9]. The model parameters for each of the seven environments appear in Table II.

B. The reference impulse response model

Our model for the reference impulse response $\tilde{h}(t)$ valid at d_0 essentially follows from (1) by exchanging a_{jk} with $\tilde{a}_{jk}$:

$$\tilde{h}(t) = \sum_{j=1}^{\infty} \sum_{k=1}^{\infty} \tilde{a}_{jk} e^{j\varphi_{jk}} \delta(t - \tau_{jk}) \tag{9}$$

It partitions the arrivals indexed through k into *clusters* indexed through j, as illustrated in Fig. 2(a) for a recorded impulse response in *Oil Refinery*. The notion of clusters harkens back to the well-known phenomenon first witnessed in [10] caused by larger scatterers in the environment which induce a group delay in the resultant

[3]Dense piping presented an environment similar to inside–outside, as discussed in [6].

[3]The *Republic Plaza* is a high-rise building located in the downtown metropolitan area.

[4]There are alternative definitions to ours for the pathgain as summarized in [4].

[5]Robust fitting henceforth denotes the Trust-Region method explained in [7].

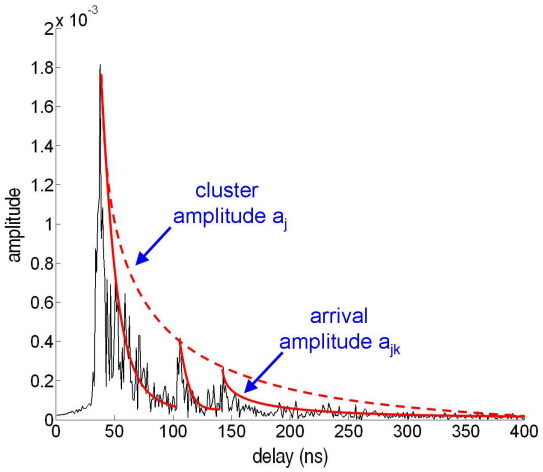

(a) Three distinct clusters in *Oil Refinery*

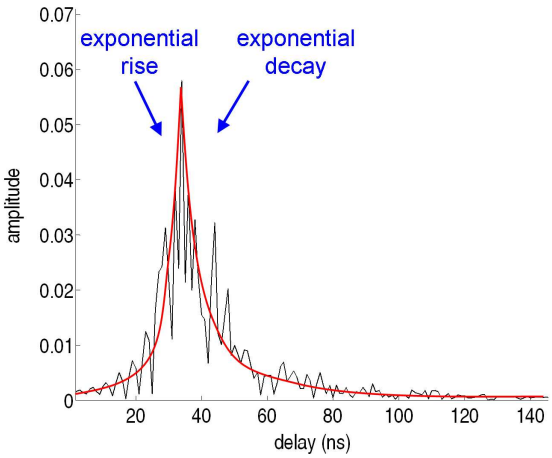

(b) Exponential rise and decay in the first cluster in *NIST Lab*

Fig. 2. The channel impulse response.

arrivals with respect to those of the first cluster. We identified the clusters visually.

In order to extract the parameters of the model, $\tilde{h}(t)$ was computed for each experiment through the IDFT in (3) for f = 698–806 MHz. However, the recorded frequency response was first normalized by the pathgain factor, replacing it instead with $\tilde{H}(f) = H(f) \Big/ \left(\frac{d}{d_0}\right)^{-\frac{n}{2}}$. Note that the parameters of the pathgain model in the previous subsection are needed in this step and so were extracted beforehand. As the receiver was placed indoors in all but *Oil Refinery*, the smaller indoor dimensions caused the arrivals to appear faster than the conventional delay resolution $\frac{1}{B}$ of the IDFT for B = 108 MHz. As a result, we chose to implement the super-resolution algorithm in [3] to generate a pseudospectrum in the place of $\tilde{h}(t)$. From it, the arrival delays τ_{jk} were extracted followed by the least-squares fit in [11] to estimate $(\tilde{a}_{jk}, \varphi_{jk})$. The latter also estimates the number of arrivals automatically through a minimum description length criteria as opposed to arbitrary selection above a certain amplitude threshold.

1) The delay τ_{jk}:

The equations in (10) govern the *arrival delays*. The ground-truth delay τ_0 in (10a) is the time elapsed for the signal to travel the distance d at the speed of light c. The *inter-cluster delay* between the first cluster and the ground-truth delay $\tau_1 - \tau_0$, as well as between the other clusters $\tau_j - \tau_{j-1},\ j \geq 1$, depends on the randomly located larger scatterers in the environment such as doors and hallways. The widely accepted Saleh-Valenzuela (S-V) model proposes that the inter-cluster delay obeys the Exponential Distribution [8], [10], [12], [13]; we believe that this consensus is rather an artifact of small measurement bandwidth coupled with conventional IDFT techniques which place the sub-resolution delays within the smallest bin by default, neglecting the distribution within this bin and in turn aritifically inflating its concentration with respect to the others; this lends the overall distribution a seemingly exponential appearance. As some other authors [14], [15], we found through using super-resolution techniques that the Weibull Distribution

$$\mathcal{W}(\tau_j - \tau_{j-1}; \Lambda, \mathcal{K}) = \frac{\mathcal{K}}{\Lambda}\left(\frac{\tau_j - \tau_{j-1}}{\Lambda}\right)^{\mathcal{K}-1} e^{-\left(\frac{\tau_j - \tau_{j-1}}{\Lambda}\right)^{\mathcal{K}}},$$

which reduces to the Exponential Distribution for $\mathcal{K}$ = 1, allows a more exact fitting of the curve to the data for $(\tau_j - \tau_{j-1})$ in (10b). Likewise the *inter-arrival delay* $(\tau_{jk} - \tau_{j,k-1})$ between arrivals within cluster j also obeys the Weibull Distribution in (10c) due to randomly located smaller scatterers such as furniture, as shown for *Oil Refinery* in Fig. 3.

$$\begin{aligned} &(a)\ \tau_0 = \frac{d}{c}; \\ &(b)\ (\tau_j - \tau_{j-1}) \sim \mathcal{W}(\tau_j - \tau_{j-1}; \Lambda, \mathcal{K}),\ j \geq 1 \\ &(c)\ (\tau_{jk} - \tau_{j,k-1}) \sim \mathcal{W}(\tau_{jk} - \tau_{j,k-1}; \lambda, \kappa),\ j \geq 2 \\ &\quad \tau_{j1} = \tau_j \end{aligned} \tag{10}$$

In order to fit the parameters of the distributions, the clusters were first isolated visually from the multipath profile of each experiment and indexed according to the cluster delay τ_j. The two parameters of the Weibull distribution were then robust fit to the inter-cluster delays given from all the experiments in a particular environment; in the same manner, the two parameters were fit to all the inter-arrival delays.

2) The complex reference amplitude $\tilde{a}_{jk}e^{j\varphi_{jk}}$:

In the original S-V model and in reference to Fig. 2(a), the *cluster amplitude* $\tilde{a}_j$ fades exponentially versus the

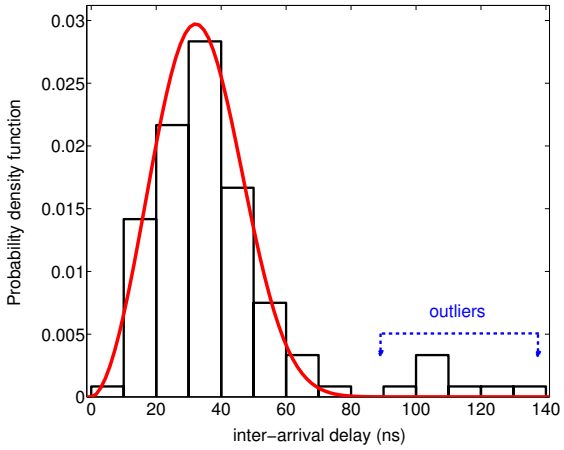

Fig. 3. Distribution of the inter-arrival delays $(\tau_{jk} - \tau_{j,k-1})$ in *Horizon West Apartments* according to the Weibull probability density function.

cluster delay τ_j according to the *cluster decay constant* $\Gamma(\tau_j)$ in (11a) for $\Gamma_1 = -1$. We found that allowing $\Gamma_1 \geq 0$ gives a better fit as illustrated in (dB) for *Oil Refinery* in Fig. 4(a), showing that the cluster amplitude in fact fades slower than exponential, with variation from the curve s_Γ. Also in the original model and as displayed in Fig. 2(a), the *arrival amplitude* $\tilde{a}_{jk}$ fades exponentially versus the *intra-cluster delay* $(\tau_{jk} - \tau_j)$ according to the *arrival decay constant* $\gamma(\tau_j)$ in (11b) for $\gamma_1 = \gamma_2 = 0$. Some researchers [8], [12], though, have found $\gamma(\tau_j)$ to be a function of the cluster delay τ_j and so have allowed $\gamma_1 = 1$; we found that unrestricting γ_1 gives an even better fit with variation from the curve s_γ, as illustrated for *Oil Refinery* in Fig. 4(b). Finally, the arrival phase φ_{jk} in (11c) is well-established in literature as uniformly distributed [3].

$$
\begin{aligned}
&(a)\ \tilde{a}_j = \tilde{a}_0 \cdot 10^{-\frac{1}{2}\frac{\Gamma(\tau_j)}{10}}; \\
&\quad \Gamma(\tau_j) = \frac{1}{\Gamma_0}\left(\frac{\tau_j}{ns}\right)^{-\Gamma_1} + s_\Gamma, \\
&\quad s_\Gamma \sim \mathcal{N}(s_\Gamma; 0, \sigma_\Gamma)
\end{aligned}
\tag{11}
$$

$$
\begin{aligned}
&(b)\ \tilde{a}_{jk} = \tilde{a}_j \cdot 10^{-\frac{1}{2}\frac{\gamma(\tau_j)(\tau_{jk}-\tau_j)+s}{10}}; \\
&\quad \gamma(\tau_j) = \frac{1}{\gamma_0}\left(\frac{\tau_j}{ns}\right)^{-\gamma_1} + \gamma_2 + s_\gamma, \\
&\quad s_\gamma \sim \mathcal{N}(s_\gamma; 0, \sigma_\gamma), \\
&\quad s \sim \mathcal{N}(s; 0, \sigma)
\end{aligned}
$$

$$
(c)\ \varphi_{jk} \sim \mathcal{U}(\varphi_{jk}; 0, 2\pi)
$$

In order to determine the parameters in (11a-b), assuming an exponential decay for the arrival amplitude as explained above, we equivalently robust fit a line to it in (dB) in Fig. 4(c) with s capturing the variation from the curve. Each fit in turn yields a data point for both the cluster amplitude in Fig. 4(a) and the arrival decay constant in Fig. 4(b) versus the cluster delay τ_j. Subsequently, we robust fit the curves shown to the data points collected from all the clusters in order to extract $(\Gamma_0, \Gamma_1, \sigma_\Gamma)$ and $(\gamma_0, \gamma_1, \gamma_2, \sigma_\gamma)$ respectively.

In *NIST Lab* and *Republic Plaza*, there is virtually no penetration of the direct path given the density of the building materials and so the first cluster in particular experiences a strong exponential rise to the peak, typical of non line-of-sight conditions, before the normal decay of the arrivals. This exponential rise can be modeled in the same manner as the decay through (11b), however by replacing $(\gamma_0, \gamma_1, \gamma_2)$ with $(\gamma_0^+, \gamma_1^+, \gamma_2^+)$ = (-7.294e-5, 1.941, 1.890e-2) and (-1.304e-1, 0.116, 4.260) in *NIST Lab* and *Republic Plaza* respectively. Fig. 2 highlights a recorded impulse response with an exponential rise in the first cluster in *NIST Lab* (b) in comparison to one without in *Oil Refinery* (a).

C. Reconstructing the impulse response

A stochastic impulse response can be reconstructed from our model through the following steps:

1) Select d (and in turn $\tau_0 = \frac{d}{c}$) and the parameters from one of the seven environments in Table II;
2) Generate the stochastic variables $(\tilde{a}_{jk}, \varphi_{jk}, \tau_{jk})$ of the arrivals from the reference impulse response model in Section IV-B: set $\tilde{a}_0 = 1$ in (11a) and then normalize the amplitudes to satisfy (7b), keeping only those clusters and arrivals with amplitude above some threshold;
3) Choose a subband in f = 698–806 MHz with bandwidth B and center frequency f_c, and sample interval Δf; compute $H(f)$ in (2) for each sample frequency from the pathgain model in Section IV-A and the generated arrivals;
4) Compute the sought impulse response $h(t)$ through (3).

V. Conclusions

In this paper, we have proposed a channel propagation model for the 700 MHz band in seven environments. The stochastic model is described through a channel impulse response complete with 17 parameters extracted from data collected from 89 transmitter-receiver configurations using the stepped-frequency measurement technique. Ours breaks from the original Saleh-Valenzuela model to evidence a slower than exponential decay in the cluster amplitude as well as an exponential decay in the arrival amplitude dependent on the cluster delay. In addition, we employed a super-resolution algorithm as opposed to the conventional Inverse Discrete Fourier Transform to expose that the inter-arrival delays are actually Weibull distributed.

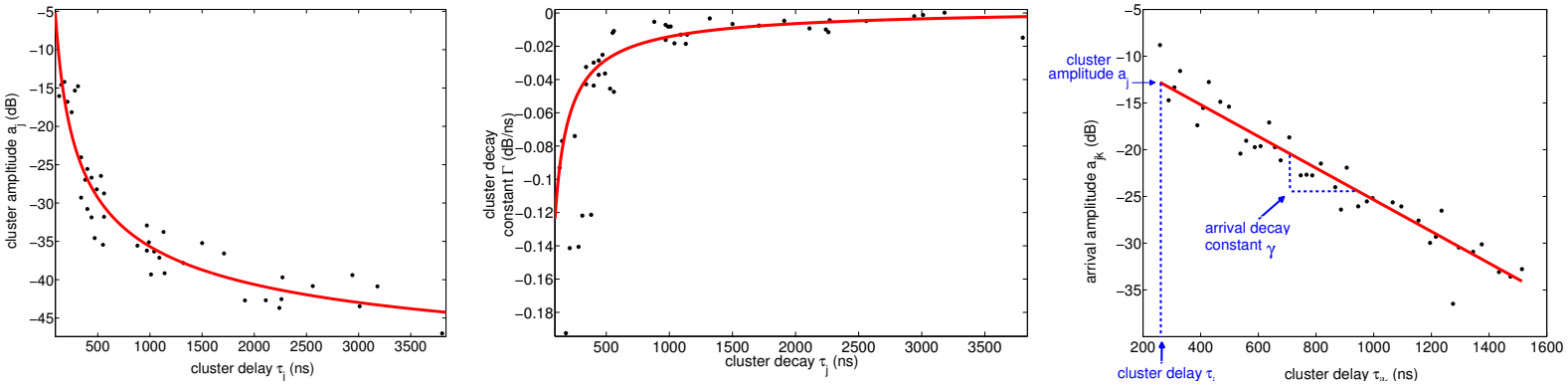

(a) Cluster amplitude (b) Decay constant (c) Arrival amplitude

Fig. 4. Parameter fitting for the reference amplitude $\tilde{a}_{jk}$.

TABLE II

THE PARAMETERS OF THE PROPOSED CHANNEL PROPAGATION MODEL FOR THE SEVEN ENVIRONMENTS

environment	pathgain					delay				amplitude							
	$PG(d_0)$ (dB)	n_0	n_1	d_1 (m)	σ_d (dB)	Λ (ns)	K	λ (ns)	κ	Γ_0 (1/dB)	Γ_1	σ_Γ (dB)	γ_0 (ns/dB)	γ_1	γ_2 (dB/ns)	σ_γ (dB)	σ (dB)
Oil Refinery	-17.90	0.35	6.62	87	1.94	883.94	1.57	54.04	3.00	-1.806e-3	0.366	6.35	2.030e-3	1.615	4.604e-3	0.033	2.79
Greathouse Mine Tunnel	-18.47	0.55	19.04	70	0.53	154.63	15.17	38.05	2.70	1.204e2	-1.451	13.49	4.604e-2	0.004	2.114e1	0.097	1.56
Hazel-Atlas Mine Tunnel	-12.23	0.26	21.19	60	2.49	∞	1	34.34	3.22	1.170e9	-3.799	5.16	8.496e-1	0.012	-9.546e-1	0.042	3.45
Horizon West Apartments	-21.66	1.82	NA	NA	4.84	565.70	2.66	42.36	4.51	-1.442e-3	0.044	5.05	2.772	-0.110	-1.446e-1	0.023	3.00
NIST Lab	-77.02	4.33	NA	NA	3.18	396.34	1.89	42.73	3.71	-4.003e-4	0.699	3.80	6.702e-5	2.309	1.915e-1	0.014	2.58
Republic Plaza	-57.17	5.95	NA	NA	3.02	582.97	1.49	37.40	4.02	-8.244e-4	0.655	7.79	1.664e-1	1.123	1.779e-2	0.011	3.38
Convention Center	-118.20	7.26	NA	NA	5.12	591.05	3.69	35.76	3.63	-2.942e-4	0.004	4.14	3.298	0.393	-2.615e-3	0.010	3.38

REFERENCES

[1] D.C. Sicker and C. Doerr, "The 700 MHz Auction," *Sensor, Mesh and Ad Hoc Communications and Networks*, pp. 1-6, June 2008.

[2] O. Malik, "700 MHz Explained in 10 Steps," *Gigaom*, March 2007.

[3] X. Li. and K. Pahlavan, "Super-Resolution TOA Estimation With Diversity for Indoor Geolocation," *IEEE Trans. on Wireless Communications*, vol. 3, no. 1, Jan. 2004.

[4] R. Vaughan and J.B. Andersen, "Channels, Propagation and Antennas for Mobile Communications," *IET Electromagnetic Wave Series 50*, Appendix A, 2003.

[5] W.F. Young, K.A. Remley, J. Ladbury, C.L. Holloway, C. Grosvenor, G. Koepke, D. Camell, S. Floris, W. Numan, and A. Garuti, "Measurements to Support Public Safety Communications: Attenuation and Variability of 750 MHz Radio Wave Signals in Three Large Building Structures," *NIST Technical Note 1552*, To be published in 2009.

[6] K.A. Remley, G. Koepke, C.L. Holloway, C. Grosvenor, D. Camell, J. Ladbury, D. Novotny, W.F. Young, G. Hough, M.D. McKinley, Y. Becquet, J. Korsnes, "Measurements to Support Broadband Modulated-Signal Radio Transmissions for the Public-Safety Sector," *NIST Technical Note 1546*, April 2008.

[7] Branch, M.A., T.F. Coleman, and Y. Li, "A Subspace, Interior, and Conjugate Gradient Method for Large-Scale Bound-Constrained Minimization Problems," *SIAM Journal on Scientific Computing*, vol. 21, no. 1, pp. 1-23, 1999.

[8] D. Cassioli, M.Z. Win, and A.F. Molisch, "The Ultra-Wide Bandwidth Indoor Channel: From Statistical Model to Simulations," *IEEE Journal on Selected Areas in Communications*, vol. 20, no. 6, Aug. 2002.

[9] A. Sibille, "Time-Domain Diversity in Ultra-Wideband MIMO Communications," *EURASIP Journal on Applied Signal Processing*, vol. 3, pg. 316-327, 2005.

[10] A. Saleh and R.A. Valenzuela, "A statistical model for indoor mulipath propagation," *IEEE Journal on Selected Areas of Communications*, vol. 5, pp. 128-137, Feb. 1987.

[11] H. Yamada, M. Ohmiya, Y. Ogama, and K. Itoh, "Superresolution techniques for time-domain measurements with a network analyzer," *IEEE Trans. on Antennas and Propagation*, vol. 39, pp. 177-183, Feb. 1991.

[12] A.F. Molisch, K. Balakrishnan, D. Cassioli, C.-C. Chong, S. Emami, A. Fort, J. Karedal, J. Kunisch, H. Schantz, U. Schuster, and K. Siwiak, "A Comprehensive Model for Ultrawideband Propagation Channels," *IEEE Global Communications Conf.*, pp. 3648-3653, March 2005.

[13] S.S. Ghassemzadeh, L.J. Greenstein, T. Sveinsson, A. Kavcic, and V. Tarokh, "UWB Delay Profile Models for Residential and Commercial Indoor Environments," *IEEE Trans. on Vehicular Technology*, vol. 54, no. 4, July 2005.

[14] R. Kattenbuch, "Statistical Distribution of Path Interarrivaltimes in Indoor Environment," *IEEE Vehicular Technology Conf.-Spring*, pp. 548-551, May 1998.

[15] P. Yegani and C.D. McGillem, "A Statistical Model for the Factory Radio Channel," *IEEE Trans. on Communications*, vol. 39, no. 10, pp. 1445-1454, Oct. 1991.